Electronic Supporting Information

Title: The role of the $CeO_2/BiVO_4$ interface in optimized Fe-Ce oxide coatings for solar fuels photoanodes

A. Shinde, G. Li, L. Zhou, D. Guevarra, S. K. Suram, F. M. Toma, Q. Yan, J. A. Haber, J. B. Neaton, and J. M. Gregoire

Experimental Details:

X-ray fluorescence (XRF) spectroscopy was measured on duplicate libraries deposited on Si (without $BiVO_4$) due to the overlap between the Ce L_α line (4.839 kV) from the coating and the V K_α line (4.952 kV) from the $BiVO_4$. The x-ray beam was approximately 2 mm in diameter. Since the XRF sampling depth far exceeds the film thickness, XRF counts for each element were assumed to be proportional to the number of corresponding atoms present in the coating, and the sensitivity factor for each element was calibrated using commercial XRF calibration standards (MicromatterTM). We note that the XRF calibration may result in overestimation of the Fe-Ce loading because the sputtered coatings are on the order of 1000 times thinner than the calibration standards and thickness-dependent attenuation of XRF signals was not accounted for in data processing. The bulk Fe_2O_3 and CeO_2 densities were used to calculate the nominal thickness of the coatings.

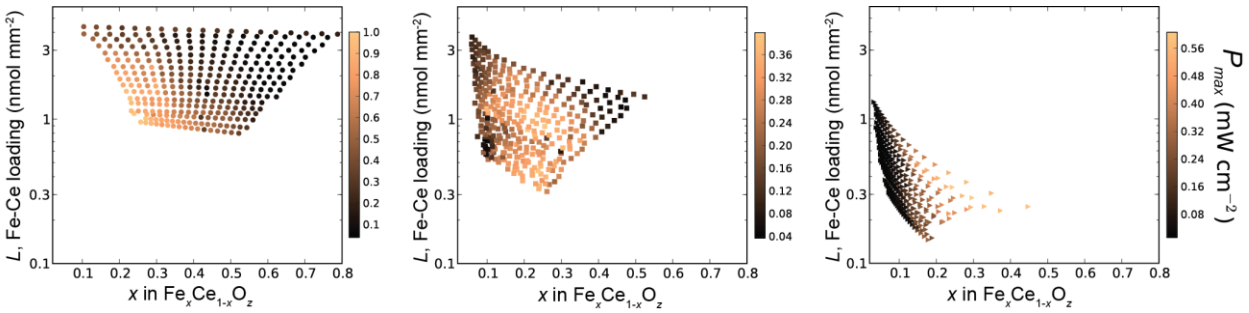

Figure S1. The maps of P_{max} from libraries A, B, and C (left to right) with common axes to visualize the different composition-loading spaces covered by these 3 libraries.

Figure S1 shows the maps of P_{max} for libraries A, B, and C, and each dataset was normalized by its maximum value to create Figure 3. The $BiVO_4$ films prepared for each library were synthesized in separate experiments from each other and additionally experienced slightly different thermal histories, resulting in different baseline photoactivities of the $BiVO_4$ and hampering comparison of absolute P_{max} values among the 3 libraries.

The *x*-*L* space of Library B encompasses the highest performing coatings, and a representative sample ($Fe_{0.26}Ce_{0.74}O_z$, 0.89 nmol mm^{-2}) was chosen for stability characterization, as shown in Figure S2.

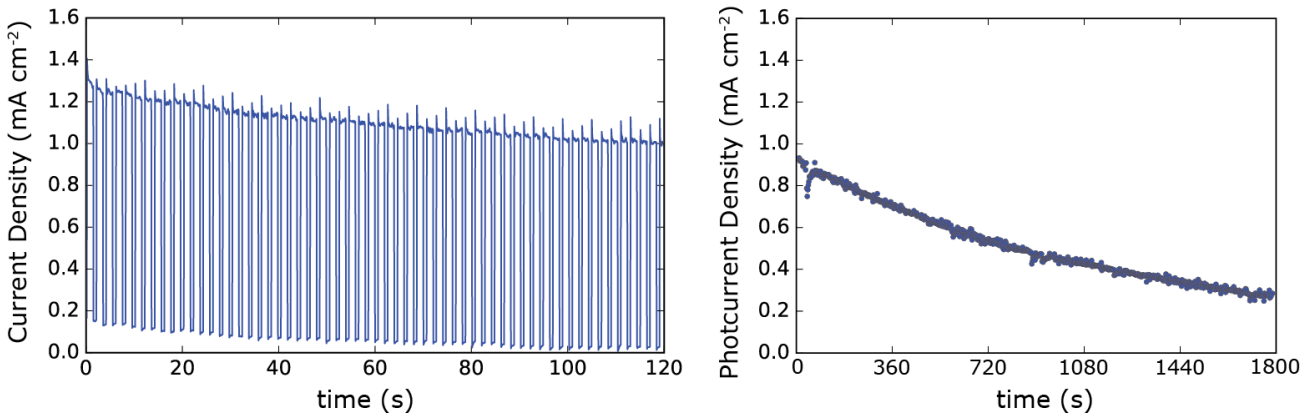

Figure S2. Stability evaluation of the $Fe_{0.26}Ce_{0.74}O_z$ and 0.89 nmol mm^{-2} sample from Library B. The series of toggled-illumination chronoamperometry experiments was performed using the same PEC instrument described in the manuscript and at 0.74 V vs RHE, which is approximately the potential that provided the maximum power in the CV. The measurements were performed after the high throughput CV experiments described in the manuscript and the sample was exposed to electrolyte solution for hours and to ambient air for days before each measurement. The 120 s experiment (left) was performed first and the raw signal from the 0.5 Hz illumination toggling is shown. The subsequent experiment (right) employed the same illumination toggling and the photocurrent (calculated as described in the manuscript) is shown over the 30 minute measurement. For reference, the photocurrent of $BiVO_4$ at this potential is approximately 0.1 mA cm^{-2} (see Fig 2). The slow degradation in photoactivity is likely due to corrosion of the underlying $BiVO_4$ via electrolyte penetration through gaps in the Fe-Ce oxide coating, motivating development of more conformal coatings with the optimal composition and loading identified in the present work.

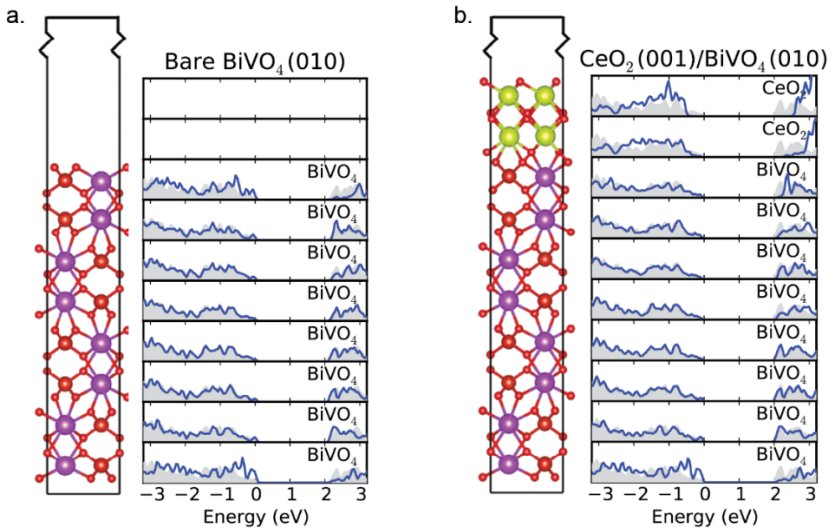

Figure S3. The model cell and the PDOS for each monolayer for (a.) defect-free $BiVO_4$ and (b.) $CeO_2/BiVO_4$, where the bottom 4 layers of each cell are fixed to bulk $BiVO_4$ lattice parameters. The shaded gray in each plot is the PDOS signal for bulk $BiVO_4$. The VBM is set to 0 eV.

The left panel of Figure S3 (a) shows the atomic structure of a defect-free $BiVO_4$(010) slab. In this slab, the bottom four monolayers of the slab are fixed to the bulk structure, while the top four monolayers are fully relaxed. In the layer PDOS, shown in the right panel of Figure S3 (a), we find the PDOS of the top and bottom layer are very similar, implying the effect of structural relaxation on the surface states is negligible.

For comparison, we show the structure and layer PDOS of $CeO_2/BiVO_4$ in Figure S3 (b), revealing that the coating of a CeO_2 epitaxial layer removes the surface states of $BiVO_4$ and makes the electronic structure of the $BiVO_4$ layer at the interface nearly identical to that of a bulk layer.

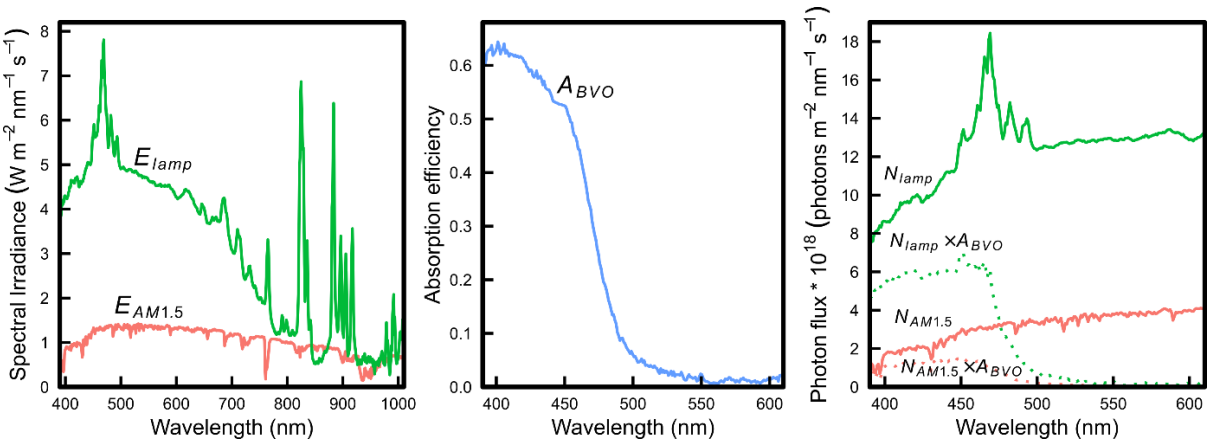

Figure S4. (left) Spectral irradiance of the xenon lamp used in the SDC experiments (green, E_{lamp}) and ASTM 6173-03 standard for global air mass 1.5 (red, $E_{AM1.5}$). (middle) Fractional absorption spectrum of the $BiVO_4$ (BVO) light absorber characterized using a dual-integrating sphere system that measures the total spectral transmission and reflection. (right) Photon flux of the xenon lamp and AM1.5 (solid lines) and photon flux of each absorbed by BVO (dotted lines).

Figure S4 shows the calibration of the illumination source (xenon lamp) used in the SDC experiments. The irradiance of the xenon lamp exceeds that of AM1.5, particularly in the ultraviolet region where $BiVO_4$ is highly absorbing. To calculate the illumination enhancement compared to AM1.5, the photon flux absorbed by $BiVO_4$ was integrated in the 390-600 nm range for the xenon lamp and AM1.5, respectively. The photon flux differs by a factor of 4.0±0.6, with uncertainty due to the lamp calibration procedure. This calibration provides a first-order approximation to adjust for $BiVO_4$-absorbable lamp irradiance: the current density for each photoanode under AM 1.5 illumination will be approximately a factor of 4 lower than that measured in the SDC experiments.